A Novel Damage Index for Online Monitoring of RC Slabs under Monotonic Loading by Integration of Process Controlling into Acoustic Emission Technique

A Novel Damage Index for Online Monitoring of RC Slabs under Monotonic Loading by Integration of Process Controlling into Acoustic Emission Technique

Arash Behnia[1], Hwa Kian Chai[2], Ahmad A. Mousa[1], Seyed Alireza Ravanfar[a]

[1] Discipline of Civil Engineering, School of Engineering, Monash University, Sunway Campus
[2] Civil and Environmental Engineering, School of Engineering, University of Edinburgh, United Kingdom

Abstract

This study introduces a novel structural health monitoring scheme for cementitious composite slabs with the aid of acoustic emission (AE) technique coupled with statistical process controlling (SPC) method. The adopted framework is an integrated monitoring solution that effectively relates current state (damaged) to reference state of the structure. Evaluation of the latter was made possible using autoregressive model incorporating a set of damage-sensitive feature. In order to provide a benchmark damage indicator, the collected data were processed using control chart analysis. The damage indicators for the former was similarly obtained and then compared with the benchmark to gauge the structural damage. These control charts offer a robust framework meticulously identifying inconsistency in the damage-sensitive feature imposed over the monitoring period. Linear and quadratic projections were also incorporated into SPC model to enhance identification of system transition to other damage states.

Keywords: Structural health monitoring; composite concrete slabs; statistical process control; acoustic emission; autoregressive model

1. INTRODUCTION

The use of composite materials is ubiquitous in civil structures due to the opportunities they offer for weight reduction [1]. Multi-layer cementitious composite slab, being a recognized composite structure, has drawn a growning attention for its cost effectiveness, raw material availability,

simple fabrication and convenient installation (regardless of shape complexity) [2]. Inherent physical properties of cementitious provide a refined material performance in terms of enhanced resistance against shrinkage and cracking, and high level of ductility [3]. Driven by potential inherent defects, the demand for safe performance over the lifetime of composite structures, however, necessitates taking rigorous monitoring measures. Hence, it is essential that reliable diagnosis and monitoring techniques be developed for continuous assessment of the structural health condition. To this end, the application acoustic emission (AE) appears to be a robust technique for structural damage diagnosis and reliability analysis for composite structures [4-7].

AE was used in localization of damage in composite and RC structures [8], prediction of delamination in composite structures [9], crack detection [10], damage assessment [11-12], corrosion, fatigue, creep, fracture modes analysis, and durability [13-19]. The premise of AE refers to the generation of transient elastic waves during the rapid release of energy from a localized source within a material. AE is a non-destructive testing technique with several unique features including real time monitoring capability, high sensitivity, global monitoring capability, source location, sensitivity to processes or mechanisms that generates stress waves, and passive nature (utilizing energy generated by damage source omits the need for supplying external energy) [20-23]. These features allow employment of AE as an informative online assessment technique for a wide range of structures and for various purposes.

To this end, few studies, if any, have developed a robust method to introduce a damage-sensitive feature from AE response in time domain data. It should be noted that because AE damage detection technique relies on experimental data with high level of uncertainty (other than environmental effects), utilization of statistical analysis procedures seems to be very efficient if quantification of damage from changes imposed to AE response is required. The inherent complex

nature of cementitious composite materials further fuels this uncertainty in monitoring structural health. With these concerns in perspective, this study innovatively utilizes AE technique to provide a comprehensive damage detection scheme and reliability analysis for structures in real time. The principal objectives of this study are twofold: introducing suitable damage-sensitive features and providing a statistical framework to monitor any inconsistency and outlier data as an indication of damage other than quantification of damage. In doing so, an autoregressive (AR) model is integrated with exponentially weighted moving average (EWMA) and Shewhart control charts to present a damage detection scheme for multilayer cementitious composite slabs.

2. EXPERIMENTAL PROGRAMS

2.1. Materials

2.1. Cementitious and Aggregate Constituents

Locally sourced ASTM Type I Portland Cement (PC) was used as the key binder material. Low calcium fly ash (class F) used in this research was supplied by Lafarge Malayan Cement Bhd, Malaysia. Due to the round particle shape and high silica content, incorporation of fly ash has the potential to reduce the water demand, enhance workability of the fresh matrix and improve the hydration process of Portland cement. Locally available river sand with grading in accordance with the limit values specified by BS882 [24] was used in the mortar mixes. The river sand was washed prior to mixing to remove potentially present natural fines (silt particles and clay lumps) in the raw stock pile.

2.1.2. Reinforcing Component

A total of six layers of welded galvanized steel square mesh with a wire diameter of 1 mm and spacing of 13 mm served as internal reinforcement for each fabricated cementitious slab. The mesh was tested in the laboratory according to the design guide on construction and repair of cementitious reported by the ACI Committee 549 [25]. The average yield and ultimate strength of the wire mesh were found to be 300 MPa and 335 MPa, respectively.

2.2. Specimen Preparation and Testing Method

The prepared mortar was poured into open top and bottom steel moulds with dimensions of 500 mm x500 mm x30 mm. For each slab specimen, a thin layer of mortar was initially poured to achieve the desired cover thickness prior to positioning the bottom wire mesh inside the mould. This is followed by casting the slab, and placing the top wire mesh. The mortar was evenly spread into the reinforcement network. In the last step, finishing was performed by applying a thin layer of mortar to ensure a smooth and levelled top surface. The specimens were left for 24 hours to set after casting. The testing machine and schematic of the test procedure are shown in Figure 1. Further detailed on specimen preparation are presented in reference 1.

2.3. Acoustic Emission Instrumentation

The AE measurement system adopted in the experimental study consisted of PCI-2 data acquisition boards (by Mistras Group Inc) that accommodate a total of six AE sensors mounted on the specimens and a operated by as AEwin Windows-based program. The AE sensors used have a resonant excitation frequency of 60 kHz (R6I). Measurements were collected for AE monitoring at a sampling rate of 2 MHz with the pre-trigger set to 250μs. The hit definition time (HDT), hit lockout time (HLT), and wave velocity were configured as 2000 μs, 300 μs and 3900 m/s,

respectively. The threshold level of acquisition was set at 50 dB to eliminate electrical and mechanical noise. However, interested readers can find the extensive and detailed information on experimental and mechanical results data in the reference 1.

3. METHODOLOGY

3.1. General Approach

This study proposes a novel and comprehensive structural health monitoring scheme in real time by integration of AE technique and statistical process controlling. To this end, six samples of two types of multi-layer composite slabs with four and six layer meshes were prepared. The slabs were tested under concentrated loads yielding two types of failure: flexural and punching. AE sensors were used to acquire AE parameters. The efficiency of AE signals were investigated for potentially serve as an efficient damage detection scheme. An autoregressive (AR) model was employed to construct a damage-sensitive feature utilizing AE energy time history, which allows identifying different damage stages. For this purpose, a cubic AR model was first examined to be used as a damage sensitive-feature. The input from the constructed AR model was used to plot control charts. Shewhart and Exponentially Weighted Moving Average (EWMA) control charts were examined to determine the efficiency of both for AE monitoring purposes. The variation in number of outliers in control charts could be used as an indication of changes in damage state. In the next step, considering the high dimensionality of the cubic AR model, linear and quadratic projections were used to transform the 3D space of the cubic AR into 1D space which can maximize the damage stages discrimination.

3.2. Statistical Process Controlling Method

The inherent AE features acquired in the experimental process, particularly for concrete structures, involves a high level of uncertainty. Therefore, statistical analysis seems to be necessary for quantifying the changes in the AE responses and correlating them with the damage state of structures. The paradigm of SPC encompasses consecutive parts: operational assessment, data acquisition and de-noising, feature extraction and –if needed– reduction of dimension [26], and implementation of statistical model [27]. The fundamentals of data feature extraction, damage sensitive feature definition, and statistical model development will be subsequently discussed.

3.3. Damage-Sensitive Feature Extraction with an AR model

The process of damage-sensitive properties extraction from the measured AE data (termed feature extraction through which one would be able to distinguish different states of damage imposed to the structure. However, distinguishing systematic differences between different damage states by the sole use of AE raw data is likely impossible. Therefore, building and using a model of AE data for damage detection purpose would be quite helpful. Generally, two key components are required to proceed with structural health monitoring (SHM) reference point state: 1. representation of AE response time history, and 2.benchmark definition.

In this study for building a model to represent AE energy response time history, AR series was designated as damage-sensitive features (model). AR shall provide a series of coefficients on which statistical procedures and analysis can be applied to establish a benchmark.

The AR model can be constructed from the time series of individual measurement point, or the spatially compressed time series data acquired form data after space reduction/projection. In the AR model of order p (AR(p)), the current point in the AE response time series is modelled as linear

combination of the previous p points. The AR time history f(t) can be mathematically expressed as follows:

$$f(t) = \sum_{j=1}^{p} \emptyset_j f(t-f) + e(t) \quad (1)$$

where f (t) is the time history at time t, $\emptyset_j$ is unknown AR coefficient, and e(t) is the random error with zero mean and constant variance. Brockwell and Davis [28] proposed a model so-called Yule-Walker to estimate $\emptyset_j$. In this study, AE energy time history was adapted in the form of several small windows by discretising the total time history into several windows. $\emptyset_j$ is accordingly computed for each time window whereby a large set of AR coefficients is generated. This large set of numbers requires the application of proper statistical model like control charts to achieve a damage diagnostic system.

3.4. EWMA and Shewhart Control Charts

Development of a proper statistical model concerns the implementation of an adequate algorithm so that analysis of distributed extracted features (AR coefficients) may result in determination of damage stages in the structure. The algorithm development in SPC can be generally considered in three different categories: classification of different groups, regression technique, and outlier detection. Proper algorithm selection may hinge on deciding upon supervised or unsupervised approach. It is noted that the supervised learning method is most appropriate when data of different damage states (intact and damaged data) are known a priori, whereas data are merely available for benchmark or undamaged stage in unsupervised methods. Within the scope of this study, a SPC model was developed for AE energy data through an unsupervised method. Control chart analysis, one of the most well-known SPC technique, was used since it is well suited for monitoring an

automated continuous system. The mean and variance of the extracted features (AR coefficient) will change if the structure under investigation experiences abnormality.

Two types of control charts, Shewhart (X-bar) and Exponentially Weighted Moving Average (EWMA) were examined to determine the efficacy of each method to monitor variation of the extracted feature means (AR coefficient means) to recognize data which are inconsistent with the past datasets. For this purpose, the features (i.e. AR coefficients) were initially rearranged in subgroups of size "n" –usually taken to be 4 or 5 as suggested by (Sohn et al) [29]. Now, let the variable ψ_{ij} denote the j^{th} feature from the i^{th} subgroup. However, other than reduced data size, using subgroups offers a significant advantage as the distribution of subgroups mean values often can be easier to approximate with a normal distribution owing to central limit theorem [29]. In the next step, means of subgroups ($\overline{X}_i$) and standard deviations of the features (S_i) were calculated in each subgroup (i = 1, …, q, in which q denotes the number of subgroups).

$$\bar{X}_i = \text{mean}(\psi_{ij}); \qquad S_i = \text{std}(\psi_{ij}) \tag{2}$$

The Shewhart X-bar control chart can be plotted through drawing a centreline (CL) at the subgroup mean with two linear bounds addressing upper and lower control limits (UCL and LCL). Centreline and corresponding boundary limits can be defined as follows:

$$\text{UCL, LCL} = \text{CL} \pm Z_{\alpha/2} \frac{S}{\sqrt{n}} \quad \text{and} \quad \text{CL} = \text{mean}(\bar{X}\text{i}) \tag{3}$$

where $Z_{\alpha/2}$ is the percentage point in the normal distribution with zero mean and unit variance so that $P[z \geq Z_{\alpha/2}]$. The total variance (S^2) is defined as the average of all subgroup variance (S^2_i): $S^2 = \text{mean}(S^2_i)$. However, the control limits of equation 3 correspond to a 100(1-α) % confidence interval if $\bar{X}$i can be approximated by a normal distribution. Finally, any outliers' occurrence by crossing the boundary limit is recorded. Exponentially Weighted Moving Average (EWMA), the

second type of X-bar control chart used in this study, is a statistic monitoring tool in which the data averaging assigns a decreasing weight to data diminishing with time.

For the Shewhart chart control method, the decision on the state of control of the process at any time "t" relies on the most recent measurement from the process and the degree of "trueness" of the estimates of the control limits from historical data. Conversely, for the EWMA control technique, the decision relies on the EWMA statistic. This follows that EWMA considers exponentially weighted average of all prior data. In general, by choosing a proper weighting factor ($\boldsymbol{\eta}$), EWMA control procedure can be built sensitive to gradual drift in the process of data. It is noteworthy that Shewhart control chart only exhibits reaction against outlier data for the last data point. The EWMA can be defined as follows [29]:

$$\text{EWMA}t = \boldsymbol{\eta}\, Yt + (1-\boldsymbol{\eta})\, \text{EWMA}t-1 \text{ for } t=1, 2,\ldots,n. \quad (4)$$

where EWMA0 is the mean of historical data (target), Yt is the observation at time t, n is the number of observations to be monitored including EWMA0 and $0 < \boldsymbol{\eta} \leq 1$ is a constant that determines the depth of memory of the EWMA. The parameter $\boldsymbol{\eta}$ controls the rate at which "older" data is presented in the EWMA statistic. A value of $\boldsymbol{\eta}=1$ suggests that only the most recent measurements impact the EWMA. Thus, a large value of $\boldsymbol{\eta}$ (closer to 1) attributes more weight to recent data and less weight to older data. Conversely, a small value of $\boldsymbol{\eta}$ (closer to 0) assigns a higher weight to older data. The value of $\boldsymbol{\eta}$ is usually taken between 0.2 and 0.3 although this is an arbitrary choice. Lucas and Saccucci [30] suggested tables that facilitate choosing of $\boldsymbol{\eta}$. The variance of EWMA (s_{ewma}^2) can be estimated as follows:

$$s_{ewma}^2 = \frac{\eta}{2-\eta} s^2 \quad (5)$$

When t (time) is not small and where s is the standard deviation calculated from the historical data the centreline would be target value or $EWMA_0$ and the boundary limits can be defined as follows:

$$UCL = EWMA_0 + ks_{ewma} \text{ and } LCL = EWMA_0 - ks_{ewma} \quad (6)$$

In the equation 6, k can be assigned a value of 3 or taken from table proposed by Lucas and Saccucci [30].

3.5 Data Compression on AR Model by Means of Linear and Quadratic Projection

The previous section explained how to plot control charts for extracted features (i.e. AR coefficients). A p-dimensional AR model can be used as a damage-sensitive feature. Therefore, for such multidimensional feature vectors, Shewhart and EWMA control chart procedures were used to discriminate feature vector by individually monitoring AR coefficients. Alternatively, AR coefficients can be monitored in simultaneous monitoring of all AR coefficients through either multivariate feature vectors or transformed one-dimensional (1D space) AR coefficient. Nevertheless, individual monitoring of multivariate feature vectors with high dimensionality might result in a huge amount of data for which visualization can be extremely difficult. Therefore, the multidimensional feature vectors will be projected onto 1D space for which SPC (control charts) can be readily applied.

In order to optimize damage states separation, feature vector transformation procedure includes linear and quadratic projection. AR coefficients will be subjected to linear and quadratic projection techniques resulting in a one-dimensional AR coefficient which will be then monitored by means of Shewhart control charts. For instance, assume there are two classes (A and B) and multidimensional feature vector x is resulted. Based on Bayes' theorem a decision boundary D(x) was proposed through which the probability of the error can be minimized [31]. As such, the

probability of misclassification refers to the reduced probability of assigning a vector to class A when it belongs to class B. The Bayes 'decision rule D(x) can be presented in a quadratic format when both classes, A and B, have normal distribution [32].

$$D(x) = x^T Q\, x + V\, x \quad (7)$$

where Q and V are quadratic and linear projection matrices, respectively. Fukunaga [32] showed that if both A and B classes have identical covariance matrices, further simplification can be applied which results in a linear form.

$$D(x) = F^T x \quad (8)$$

This decision approach can be also considered as a projection that remaps the multidimensionality of D (x) into a one-dimensional space. Therefore, a transformed feature $\psi = D(x)$ will be defined in which the means of two classes would be as far as possible while their variances are small after linear or quadratic projection. Fisher criterion [27] can be utilized to provide this projection in an optimized manner as follows:

$$f = ((m_a - m_b)^2/(\sigma^2_a - \sigma^2_b)) = ((F^T(m_a - m_b)\,(m_a - m_b)^T)F) \,/\, (F^T(\boldsymbol{\Sigma}_A + \boldsymbol{\Sigma}_B)\,F) \quad (9)$$

where m_a and m_b are the mean vectors of class A and class B distributions, $\boldsymbol{\Sigma}$A and $\boldsymbol{\Sigma}$B are covariance matrices of classes A and B, respectively, and σ_a and σ_b are the standard deviations of transformed features of classes A and B, respectively. The multidimensional feature of vector x will be correlated to the moments of projected features as follows:

$$m_i = F^T m_i \quad \text{and} \quad \sigma_i^2 = F^T\, \boldsymbol{\Sigma} F \text{ for I = A or B} \quad (10)$$

Linear projection can be obtained from derivation of "f" with respect to F that is set to zero (Bishop, 1995) which yield in equation 11

$$F = 2\,(\boldsymbol{\Sigma}_A + \boldsymbol{\Sigma}_B)^{-1}\,(ma - m_b) \quad (11)$$

If distribution of class A and B have similar covariance matrices ($\boldsymbol{\Sigma}_A$ and $\boldsymbol{\Sigma}_B$), the linear projection can be optimized. For the current test data acquired from AE responses, AE energy time history exhibited different covariance matrices in different damage states. Since in the general condition, the Bayesian decision boundary is quadratic with unequal covariance matrices, the optimized transformation might be quadratic. However, the computation of terms presented in Equation 7 (Q and V) seems more intensive than linear projection. Nevertheless, Sohn et al. [29] proposed to introduce a new variable y_i which is representative of products of two x_is. Therefore, Equation 7 can be rewritten in linearized form as follows:

$$D(x) = \sum_{i=1}^{p}\sum_{j=1}^{p} q_{ij}x_i x_j + \sum_{i=1}^{p} v_i x_i = \sum_{i=1}^{p\,(p+1)/2} a_i y_i + \sum_{i=1}^{p} v_i x_i \qquad (12)$$

where q_{ij} and v_i are components of quadratic and linear forms (Q and V), y_i denotes the product of x_js, and the corresponding entry in matric Q is denoted by a_i. As stated before, p is either the order of AR model or dimension of AR coefficients. Assume C and D represent the column vector of y_is and x_js, respectively. Then, by introducing a new variable $W = [C^T\ D^T]^T$ and taking E and S as the expected vector and covariance matric of W, respectively, the following linear equation can be written for A and V:

$$[a_1 \ldots a_{n(n+1)/2} V_1 \ldots\ldots V_n]^T = 2\,[S_A + S_B]^{-1}(E_A - E_B) \qquad (13)$$

By rearranging a_is and v_js matric Q and vector V will be obtained. In view of this, the foregoing projection technique warrant twofold objective: 1.dimension reduction and, 2. providing a discriminant function. In a broader sense, n-dimension of AR model was projected to a single space through which mean differences between damage states were maximized. Damage diagnosis technique was constructed by using SPC model applied on the transformed features.

4. RESULTS AND DISCUSSION

4.1. Mechanical Behavior of Composite Slabs

Figure 3 schematically presents two typical failure patterns for composite slabs: punching and flexure. Both failures were experimentally registered in this study. Composite slabs with four layers of wire meshes (S4) failed in flexural failure mode, whereas composite slabs with six layers of wire meshes (S6) failed in punching failure mode. As the load increased, new cracks are formed and the existing cracks slightly propagate in the radial direction. Punching failure is highlighted by a sudden drop in the applied load. As illustrated in Figure 3a, punching shear failure in the form of truncated failure cone is developed. The failure is indicated by the formation of a “hole" on the top face with a growing perimeter propagating towards the bottom face. Comparatively, when most of the reinforcement yielded prior to failure and the slabs subsequently underwent large deflection and smooth decline of carrying load, the dominant failure mode was flexural failure. In this case, cracks propagated in diagonal direction in the bottom face as illustrated in Figure 3b. Further details of mechanical results and analysis are given in reference 1.

4.2. AE Signal Energy Analysis

From the AE measurement and analysis performed on the AE data, the trend of variation of AE energy with respect to the evolution of damage was investigated. For this purpose, the largest AE energy was chosen. According to the energy level of AE hit, all AE hits were categorized into four groups (classes). There are three selected energy levels for which four associated classes can be defined as follows:

Level 1: 10000 $V^2\mu s$; Level 2= 100000 $V^2\mu s$; Level 3 = 1000000 $V^2\mu s$

Class A: under level 1; Class B: above level 1; Class C: above level 2; Class D: above level 3

The number of AE events and percentages corresponding to AE energy level released during the damage process of composite slabs relative to the associated total values are presented in Table 1 and Figure 4. As presented in Table 1 results for both composite slabs (S4 and S6) show that while the number of occurrences of AE events in class A was considerably high, the AE energy released during these AE events were significantly low. Consequently, it might be inferred that the level of damage pertinent to these AE activities is significantly low. It was observed that most AE events belonged to class B in terms of energy level. This follows that most of the signals which were emitted during the damage process had energy level greater than 100,000 $V^2\mu s$ (Level 2).

Figure 5 depicts the AE events source localization for S6 specimen during damage process considering different classes of AE energy levels. As indicated in Figure 5, AE energy level of class C contributed significantly to the fracture process zone while AE energy above Class C (Class D) possessed fairly high acoustic emission energy per unit area of fracture process zone. These observations indicate that AE events with higher energy level than 100,000 $V^2\mu s$ predominantly contributed to the fracture process zone because of their high energy level, whereas the total numbers of AE activities were quite low. The number of AE event for class A and B was considerably high while these AE events possessed low energy. Conversely, AE events intensity for class C and D were lower while associated AE energies were considerably high especially these events located in fracture zone (punching area). Therefore, it is evident that AE energy has a great potential trace changes imposed to the structure during the fracture process. Subsequently, a damage index by using AE energy time history of S6 was extended.

4.3. AE Energy Index

AE energy released during the period of loading was measured from AE acquired data set. Figure 6 displays the history of AE energy rate and history of stiffness variation for a composite slab loading set till ultimate failure. It can be observed that loading in the beginning of the test did not trigger the AE energy immediately, but rather later. It is because that fracture did not occur at the early stage of loading because the AE energy is attributed to prompt release of energy in a concrete during fracture. In addition, AE energy general trend showed a tendency to rise with increase in loading process and subsequent reduction of specimen's stiffness. The similar result was observed in the earlier work [17] which resulted in proposing a damage index by AE energy.

Figure 7 depicts the accumulated AE energy, and total and loss of stiffness values until failure. Considering the relation between accumulated AE energy and loss of stiffness, an attempt can be put forward to find out a correlation between normalized values of accumulated AE energy and loss of stiffness. The normalized accumulated AE energy and loss of stiffness over successive loading stages are plotted in Figure 8. Cumulative AE energy E_n^{AE} at time "t" the loss of stiffness (K_r/K_{ro}) were extracted and plotted in left top side of Figure 8. It should be noted that the AE energy and loss of stiffness were both normalized at the end of 50% loading process where a visible turning point was observed in total stiffness value in Figure 7.

AE energy and slab loss of stiffness in each instance were named as E^{AE} and K_r, respectively, whereas AE energy and slab loss of stiffness were named as $E0^{AE}$ and K_{r0}, respectively. AE energy attained in the present work addresses the released strain energy in concrete specimens. However, a fairly well correlation can be found in Figure 8 till 50% of loading (Stage A) between E^{AE}/E_0^{AE} and K_r/K_{r0} which is displayed in top left side of Figure 8. Therefore, the following correlation can be made for this stage:

$$E^{AE}/E_0^{AE} = K_r/K_{r0} = E_A^{AE}/E_0^{AE} = K_{rA}/K_{r0} = 1 \quad (14)$$

On the other hand, the correlation in stage B can be expressed as:

$$E^{AE}/E_0^{AE} = (\alpha)\, K_r/K_{r0} \text{ where in the end of test } \alpha \simeq 3 \quad (15)$$

However, the loss of stiffness is a significant indication of damage degree imposed to a structure. Therefore, it can be taken into account as a damage severity indicator index (DI):

$$DI = K_r/K_{ru} \quad (16)$$

At the ultimate level of damage (DI = 1), the loss of stiffness (Kr) approaches its maximum value (K_{ru}). Considering the correlation between loss of stiffness and AE energy, damage index can be postulated as following:

$$DI = (\beta)\, E^{AE}/E_u^{AE} \quad (17)$$

where $\beta = 1/\alpha$, and E_u^{AE} is the ultimate value of E^{AE} in the end of the test. It can be observed that damage index showed an admissible relation with AE energy released during the fracture in composite cementitious slabs and it could be a proper candidate for assessing the level of damage in cementitious structures. There are, however, some drawbacks toward utilizing this conventional analysis in practical applications. For example, the variable β in Equation 17 is dependent on the test condition and is not in a certain range. Secondly, this damage index can be obtained only through conducting the test until failure, which is impractical in monitoring real structures. Finally, the observed experimental repeatability in this test program does not warrant applicability under different testing conditions. On the other hand, statistical methods enable one to distinguish the pattern of complex data with enormous uncertainties by setting a reference point to discrete data distribution pattern.. Therefore, statistical process control (SPC) method is introduced hereto detect damage state by offering a reference bases unsupervised method by taking in account the AE energy data.

4.4. Feature Extraction and Damage Detection Analysis

The SPC as a damage diagnosis technique is firstly applied on the damage sensitive features (AR coefficients) and subsequently Shewhart X-bar control chart and EWMA control chart are constructed for each individual AR coefficient. In the next step, the projection technique that was explained earlier, is implemented for Shewhart X-bar control chart. In order to map multi-dimensional AR coefficients into 1D space, linear and quadratic projection are utilized through which the mean differences between data set acquired from damage states is maximized. Thereafter, SPC technique is introduced to the transformed 1D scale feature.

The 20,001-point measured AE energy time series were first divided into 1,000 20-point time windows (eliminating one-point). Third order AR model (AR (3)) was used to fit within an individual window resulting in 1,000 sets of AR coefficients. The means for 250 data subgroups of size 4 were calculated. Damage diagnosis in the form of a Shewhart control chart for the first AR coefficient is shown in Figure 9. By stetting $\alpha = 0.01$ in Equation 3 the corresponding upper and lower limits within 99%-confidence interval level were obtained. Table 2 summarizes results of different damage states obtained by EWMA and Shewhart X-bar control chart. For computing outliers in EWMA control chart, related parameters k and $\boldsymbol{\lambda}$ were set to 3 and 0.3, respectively. Subsequent damage states are plotted by means of constructed UCL, LCL, and CL. It should be noted that prior to plotting the control charts the extracted features (e.g. in Figure 9 the first AR coefficient) were first normalizing and standardized by subtracting the extracted features from the mean and standard deviation. The features were then plotted in each damage state with respect to corresponding control limits. A similar statistical approach was used to standardize the extracted features of the other damage states.

The diagnosis results obtained by other AR coefficients are shown in Table 2. As found in this case study, the third AR coefficient is the most sensitive and indicative of damage, whereas the first AR coefficient showed less sensivitiy to the damage progress. For damage level I in 750 collected samples using Shewhart and EWMA control charts , the total number of outliers are 2 (0.27%) and 7 (0.93%), respectively. However, it should be noted that the plotted control chart was constructed considering 99% of confidence interval which means features extracted from the control charts can still generate 1% outliers without indication of damage. As a result, it is not clearly certain if the system has experienced any damage at this level considering results obtained by individual AR X-bar control chart, especially Shewhart method. As could be observed in Table 2, some AR coefficients exhibit more sensitivity than others in some levels of damage and vice versa. In addition, calculating and constructing X-bar control charts for individual AR coefficients can be a non-linear process. To this end, the procedure of constructing X-bar control charts for individual AR coefficients was simplified into a single X-bar control chart of 1D space. Therefore, the projection techniques presented in previous sections were introduced to multiple space AR coefficients to transmit into 1D AR space for Shewhart X-bar control chart.

3D AR coefficients are initially projected into 1D space. The transmitted features were then used to plot X-bar control charts. In general, projection and transmission features from higher to lower order space may result in loss of information. Therefore, to overcome this problem Fisher's criterion (Equation 9) was implemented to maximize the class separation. Table 3 compares the monitoring process results using quadratic projection to that of linear projection . By comparing results obtained for multiple AR coefficient presented in Table 2 with results obtained in Table 3, the improvement in diagnosis performance is evident. The diagnosis measurements for the other specimens resulted in a similar performance improvement by using projection technique. It is

noteworthy that, in general, the linear projection might not be the optimized projection since the order of different class covariance matrices (different damage states) is different. Quadratic projection theoretically minimizes the misclassification error. In this particular case study, linear projection still shows acceptable performance while presenting results close to EWMA method.

It is evident that the quadratic technique had considerably outperforms other techniques (Figure 10). However, EWMA monitoring performance showed acceptable performance especially for those damage states of level 1, 2, and 3. Results obtained in EWMA are somewhat close to those of linear projection, especially for damage state level 1, 2, and 3. However, for the first two damage levels, similar performances were observed to a certain degree for all presented methods, whereas quadratic technique was the only reliable scheme for damage level 1 with higher outlier percentages than interval error. Relative increment in damage indicator for each stage of damage is presented in Figure 10b.Interestingly, Shewhart and linear project schemes showed lower level of increment in damage indicator for the last damage level, whereas quadratic projection kept steady incremental trend in each subsequent damage level. The increment rate for the last level of damage in EWMA scheme was similar to its damage level 3.

In order to study the effect of AR model order for Shewhart and EWMA damage monitoring schemes, the effect of three different AR orders of 3, 5, and 7 on the damage indicator values were closely examined (Figure 11). It can be observed that structural damage was successfully detected for all damaged states. The increase in damage indicators corresponding to the increase in damage severity was captured for all the damage schemes with different AR model order. The data and results obtained using AR model order of 7 indicate low sensitivity especially for Shewhart model in the last states of damage. This can be attributed to the smaller increments in damage indicator.

Results for AR model order of 3 and 5 were quite similar to those of order 7; thus, AR model order of 3 are deemed favourable for producing less volume of data in monitoring process.

CONCLUSION

In the present study, acoustic emission energy was investigated to determine appropriate damage indication parameters. AE energy time history was used as input data for an autoregressive model of order to present damage-sensitive features. Obtained damage sensitive features were used to plot different control charts to ultimately find out the relation between the variation of number of outliers and damage state in the composite slabs to conduct a statistical damage detection framework. In general, the proposed damage detection procedure provides an unsupervised scheme with introducing a benchmark to establish a comparison with the current state of the structure.

Considering the dependency of conventional AE analysis on experiment and environment parameters, the proposed method aimed to provide independent outlier parameters by proposing a benchmark for regular inspections. Hence, AR model by using AE energy data is introduced as a damage sensitive feature and by incorporating damage features into exponential weighted moving average (EWMA) and Shewhart control charts, an online monitoring framework is proposed. The following key findings can be drawn from experimental observation and analysis:

• AE events with high energy contributed in fracture process zone; therefore, AE signal energy could be adequately used as a damage index parameter to present the loss of stiffness in composite slabs.

• AR model provided a suitable damage sensitive feature of AE energy by confidence of 99%.

• Shewhart (after projection) and EWMA control charts provides a reliable statistical online monitoring framework.

• EWMA is more sensitive damage scheme compared to Shewhart control charts.

• The order of AR model could significantly affect the results of Shewhart control charts, whereas the EWMA is somewhat independent of this choice. In general, AR order of 3 gives more favourable results.

• The use of either a linear or quadratic projection technique from a 3D space into 1D space significantly improve damage diagnosis of structures.

Acknowledgment

The Authors would like to acknowledge the Ministry of Higher Education (MOHE) for providing the financial support for this project under Grant No. UM.C/HIR/MOHE/ENG/54.

References

[1] A. Behnia, N. Ranjbar, H.K. Chai, A.L. Abdullah, M. Masaeli, Fracture characterization of multi-layer wire mesh rubberized ferrocement composite slabs by means of acoustic emission, J Clean Prod. 157 (2017) 134-147. https://doi.org/10.1016/j.jclepro.2017.03.192.

[2] A. Hamoda, K.M.A. Hossain, K. Sennah, M. Shoukry, Z. Mahmoud, Behaviour of composite high performance concrete slab on steel I-beams subjected to static hogging moment, Eng Struct. 140 (2017) 51-65. https://doi.org/10.1016/j.engstruct.2017.02.030.

[3] C.B. Cheah, M. Ramli, Load capacity and crack development characteristics of HCWA–DSF high strength mortar ferrocement panels in flexure, Constr. Build Mater. 36 (2012) 348-357. https://doi.org/10.1016/j.conbuildmat.2012.05.034.

[4] D.G. Aggelis, D.V. Soulioti, N. Sapouridis, N.M. Barkoula, A.S. Paipetis, T.E. Matikas, Acoustic emission characterization of the fracture process in fibre reinforced concrete, Constr. Build Mater. 25 (2011) 4126–4131. https://doi.org/10.1016/j.conbuildmat.2011.04.049.

[5] F. Sagasta, M.E. Zitto, R. Piotrokowski, A. Benavent-Climent, E. Suarez, A. Gallego, Acoustic emission energy b-value for local damage evaluation in reinforced concrete structures subjected to seismic loadings, Mech. Syst. Signal Pr. 120 (2018) 262-277. https://doi.org/10.1016/j.ymssp.2017.09.022.

[6] A. Behnia, H.K. Chai, M. GhasemiGol, A. Sepehrinezhad, A.A. Mousa, Advanced Damage Detection Technique by Integration of Unsupervised Clustering into Acoustic Emission, Eng. Fract Mech, 2018. https://doi.org/10.1016/j.engfracmech.2018.07.005.

[7] R. Vidya Sagar, Acoustic emission characteristics of reinforced concrete beams with varying percentage of tension steel reinforcement under flexural loading, Case Stud. Constr. Mater. 6 (2017) 162-176. https://doi.org/10.1016/j.cscm.2017.01.002.

[8] M. Bagherifaez, A. Behnia, A.A. Majeed, H.K. Chai, 2014. Acoustic Emission Monitoring of Multicell Reinforced Concrete Box Girders Subjected to Torsion, The Scientific World Journal. https://doi.org/10.1155/2014/567619.

[9] M. Saeedifar, M. Fotouhi, M.A. Najafabadi, H.H. Toudeshky, Prediction of delamination growth in laminated composites using acoustic emission and cohesive zone modelling techniques, Compos. Struct.124 (2015) 120-127. https://doi.org/10.1016/j.compstruct.2015.01.003.

[10] S. Iliopoulos, D.G. Aggelis, L. Pyl, J. Vantomme, P. Van Marcke, E. Coppens, L. Areias, Detection and evaluation of cracks in the concrete buffer of the Belgian Nuclear Waste container using combined NDT techniques, Constr. Build Mater. 78 (2015) 369-378. https://doi.org/10.1016/j.conbuildmat.2014.12.036.

[11] M. Zitto, R. Piotrkowski, A. Gallego, F. Sagasta, A. Benavent-Climent, Damage assessed by wavelet scale bands and b-value in dynamical tests of a reinforced concrete slab monitored with acoustic emission, Mech. Syst. Signal Pr. 60-61 (2015) 75-89. https://doi.org/10.1016/j.ymssp.2015.02.006.

[12] A. Larosche, P. Zieh, J. Mangual, M.K. ElBatanouny, Damage evaluation of prestressed piles to cast in place bent cap connections with Acoustic Emission, Eng. Struct. 84 (2015) 184-194. https://doi.org/10.1016/j.engstruct.2014.10.026.

[13] M. Abdelrahman, M.K. ElBatanouny, P.H. Ziehl, Acoustic emission based damage assessment method for prestressed concrete structures: Modified index of damage, Eng. Struct. 60 (2014) 258-264. https://doi.org/10.1016/j.engstruct.2013.12.037.

[14] D.G. Aggelis, D.V. Soulioti, E.A. Gatselou, N.M. Barkoula, T.E. Matikas, Monitoring of the mechanical behavior of concrete with chemically treated steel fibers by acoustic emission, Constr. Build Mater. 48 (2013) 1255–1260. https://doi.org/10.1016/j.conbuildmat.2012.06.066.

[15] A. Carpinteri, A. Grazzini, G. Lacidogna, A. Manuello, Durability evaluation of reinforced masonry by fatigue tests and acoustic emission technique, Struct Control Hlth. 21 (2014) 950-961. https://doi.org/10.1002/stc.1623.

[16] A. Zaki, H.K. Chai, A. Behnia, D.G. Aggelis, J.Y. Tan, Z. Ibrahim, Monitoring fracture of steel corroded reinforced concrete members under flexure by acoustic emission technique, Constr Build Mater. 136 (2017) 609-618. https://doi.org/10.1016/j.conbuildmat.2016.11.079.

[17] A. Benavent, E. Castro, A. Gallego, Evaluation of low-cycle fatigue damage in RC exterior beam-column subassemblages by acoustic emission, Constr Build Mater 24 (2010) 1830-1842. https://doi.org/10.1016/j.conbuildmat.2010.04.021.

[18] A. Farhidzadeh, E. Dehghan-Niri, S. Salamone, B. Luna, A. Whittaker, Monitoring Crack Propagation in Reinforced Concrete Shear Walls by Acoustic Emission, ASCE J. Struct. Eng. 139 (12) (2013) 04013010. https://doi.org/10.1061/(ASCE)ST.1943-541X.0000781.

[19] Y. Kawasaki, T. Wakuda, T. Kobarai, M. Ohtsu, Corrosion mechanisms in reinforced concrete by acoustic emission, Constr. Build Mater. 48 (2013) 1240–1247. https://doi.org/10.1016/j.conbuildmat.2013.02.020.

[20] D.G. Aggelis, Classification of cracking mode in concrete by acoustic emission parameters, Mech. Res. Commun. 38 (3) (2011) 153–157. https://doi.org/10.1016/j.mechrescom.2011.03.007.

[21] A. Behnia, A. Ranjbar, H.K. Chai, M. Masaeli, Failure prediction and reliability analysis of ferrocement composite structures by incorporating machine learning into acoustic emission monitoring technique, Constr. Build Mater. 122 (2016) 823-832. https://doi.org/10.1016/j.conbuildmat.2016.06.130.

[22] N. Ranjbar, A. Behnia, H.K. Chai, J. Alengaran, Fracture evaluation of multi-layered precast reinforced geopolymer-concrete composite beams by incorporating acoustic emission into mechanical analysis, Constr. Build Mater. 127 (2016) 247-283. https://doi.org/10.1016/j.conbuildmat.2016.09.144.

[23] F.A. Uddin, M. Shigeishi, M. Ohtsu, Fracture mechanics of corrosion cracking in concrete by acoustic emission, Meccanica 41 (2006) 425–442. https://doi.org/ 10.1007/s11012-006-0004-9.

[24] BS 882:1992. Specification for aggregates from natural sources for concrete. British Standards Institution.

[25] G.B. Batson, J.O. Castro, A.J. Guerra, M.E. Iorns, C.D. Johnston, A.E. Naaman et al. Guide for the Design, Construction and Repair of Ferrocement, ACI Struct. J. 85 (3) (1988) 325-351.

[26] P. Fanning, E.P. Carden, Auto-regression and statistical process control techniques applied to damage indication in telecommunication masts, Key Eng. Mater. 204 (5) (2001) 251-260. https://doi.org/10.4028/www.scientific.net/KEM.204-205.251.

[27] C.M. Bishop, Neural Networks for Pattern Recognition, Oxford University Press, Oxford, 1995.

[28] P.J. Brockwell, R.A. Davis, Time Series: Theory and Methods, Springer, New York, 1991.

[29] B.H. Sohn, J.A. Czarnecki, C.R. Farrar, Structural health monitoring using statistical process control, ASCE J. Struct. Eng. 126 (2000) 1356-1363. https://doi.org/10.1061/(ASCE)0733-9445(2000)126:11(1356).

[30] J.M. Lucas, M.S. Saccucci, Exponentially weighted moving average control schemes: properties and enhancements, Technometrics 32 (1990) 1-12. https://doi.org/10.2307/1269835.

[31] M.L. Fugate, H. Sohn, C.R. Farrar, Vibration-based damage detection using statistical process control, Mech. Syst. Signal Pr. 15 (4) (2001) 707-721. https://doi.org/10.1006/mssp.2000.1323.

[32] K. Fukunaga, Introduction to Statistical Pattern Recognition, second ed., Academic Press, New York, 1990.

Table1: Acoustic emissions events and the recorded AE energy

	AE Energy V^2 us	AE Events		AE Energy	
		Number	Percentage %	Total AE Energy	Percentage %
S6	Total	21007	100.00	5663318794	100.00
	class A	18042	85.89	509046273	8.99
	class B	2965	14.11	5154272521	91.01
	class C	556	2.65	4159084183	73.43
	class D	47	0.22	2392668000	42.24
S4	Total	6935	100.00	36829054849	100.00
	class A	4817	69.46	259394399.2	0.70
	class B	2118	30.54	36569660450	99.30
	class C	200	2.88	36056950447	97.90
	class D	67	0.97	35212307000	95.61

Table2. Outlier of X-bar control charts by using different AR coefficients

	Damage level							
	Shewhart X-bar control chart				EWMA			
AR coefficient	Level 1	Level 2	Level 3	Level 4	Level 1	Level 2	Level 3	Level 4
α1	1/250	5/250	10/250	12/250	0/250	5/250	35/250	53/250
α2	0/250	7/250	12/250	22/250	4/250	25/250	97/250	155/250
α3	1/250	16/250	55/250	53/250	3/250	36/250	106/250	196/250
Total outliers	2/750	28/750	77/750	87/750	7/750	66/750	238/750	404/750
Percentage %	0.27	3.7	10.27	11.6	0.93	8.8	31.7	53.87

Table3. Outlier of Shewhart X-bar control chart by Linear and Quadratic projection

	Damage level							
	Linear projection				Quadratic projection			
AR coefficient	Level 1	Level 2	Level 3	Level 4	Level 1	Level 2	Level 3	Level 4
α	2/250	21/250	99/250	165/250	3/250	26/250	112/250	216/250
Percentage%	0.8	8.4	39.6	66	1.2	10.4	44.8	86.4

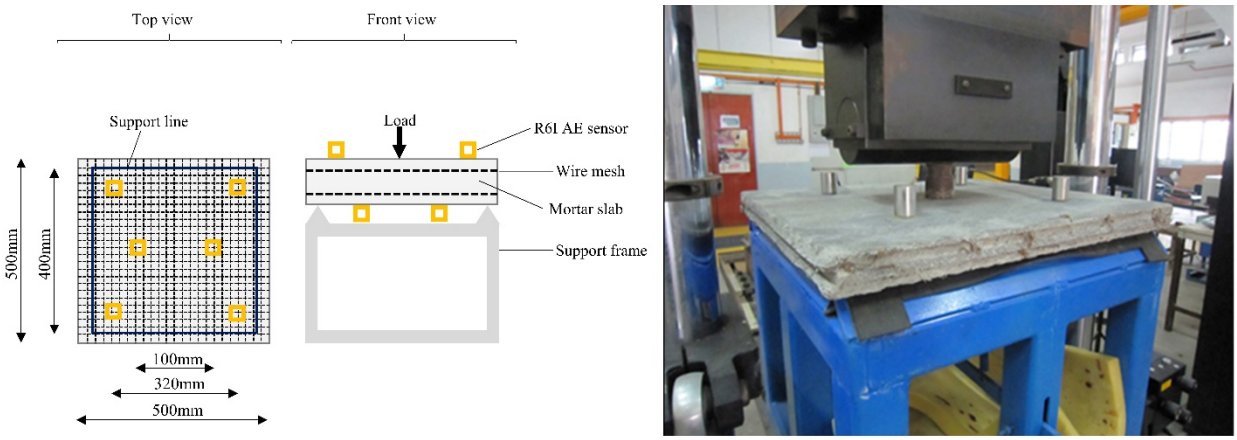

Figure 1: Test setup and AE sensor placemen

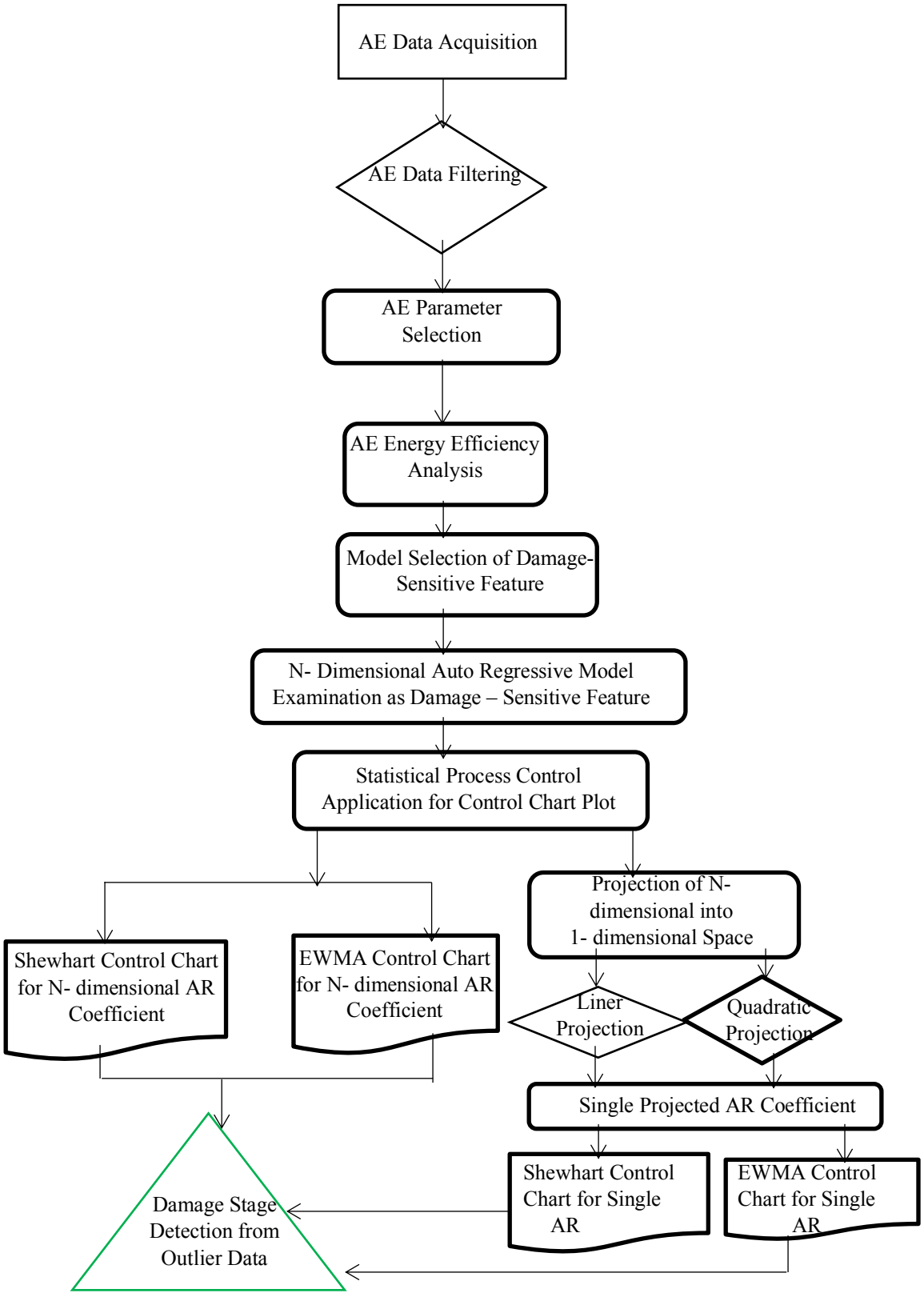

Figure 2: SHM scheme Flowchart

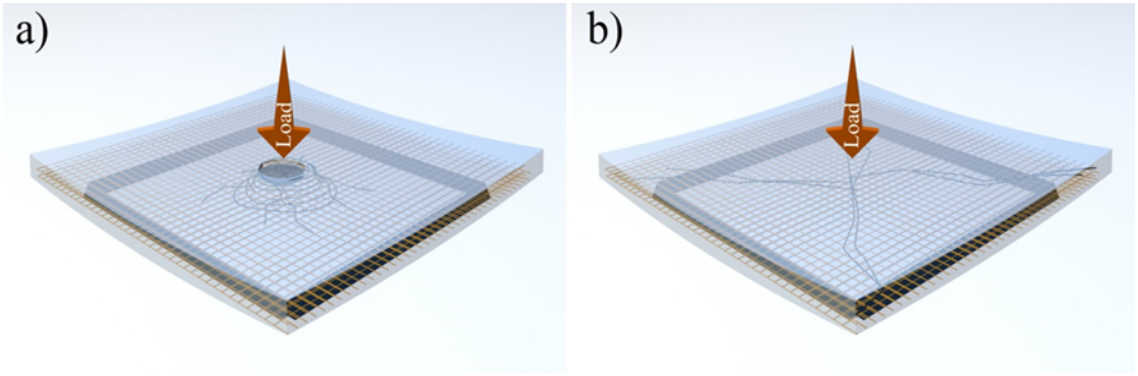

Figure 3: General types of failure modes: a) Punching failure (S6), b) Flexural failure (S4)

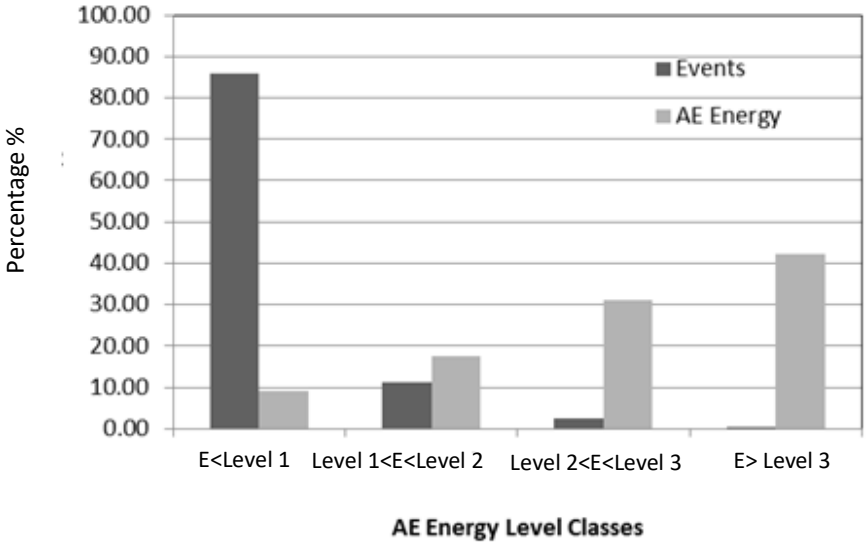

Figure 4: AE energy level distribution against AE events distribution for S6

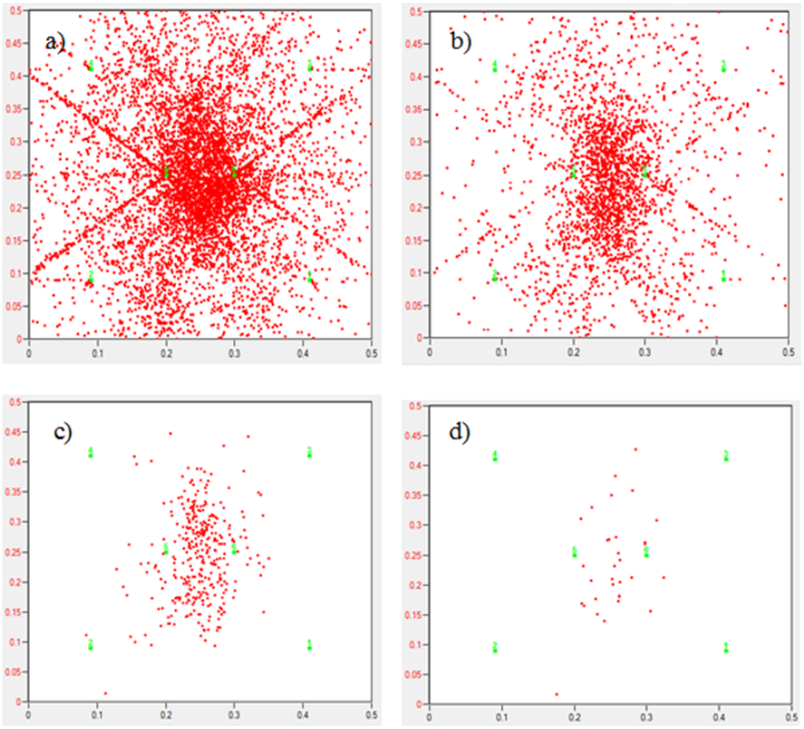

Figure 5: Acoustic emission event source localization with respect to different energy classes: a) Class A, b) Class B, c) Class C, d) Class D

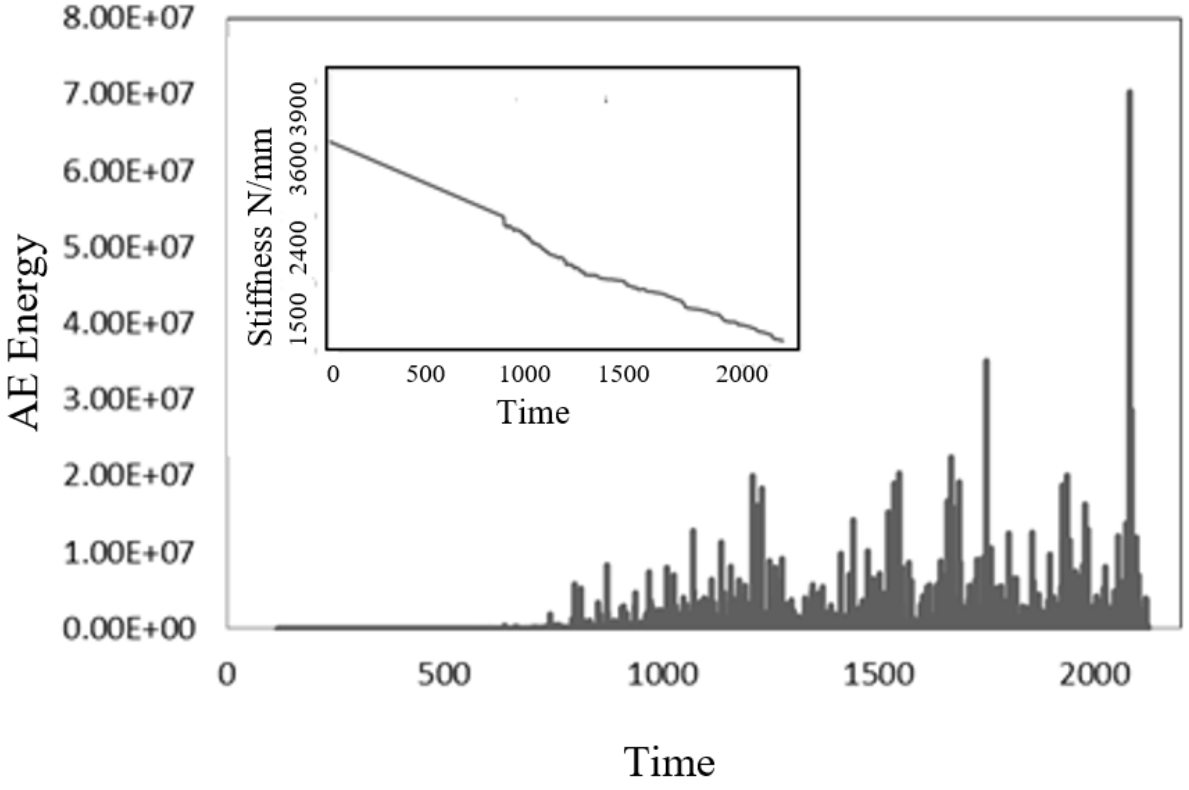

Figure 6 AE energy rate and stiffness variation time history till ultimate load capacity

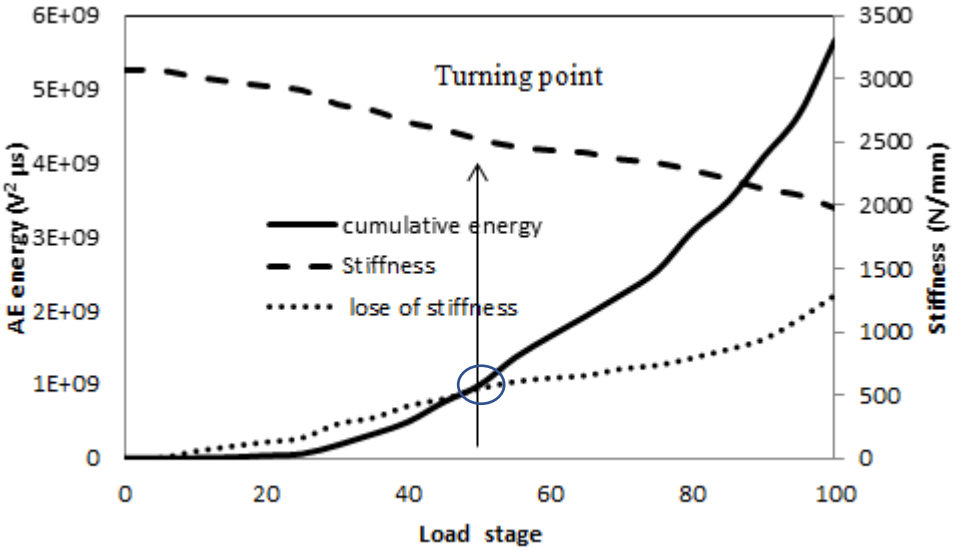

Figure 7 Accumulated AE energy during loading stage till failure and total and loss of stiffness values

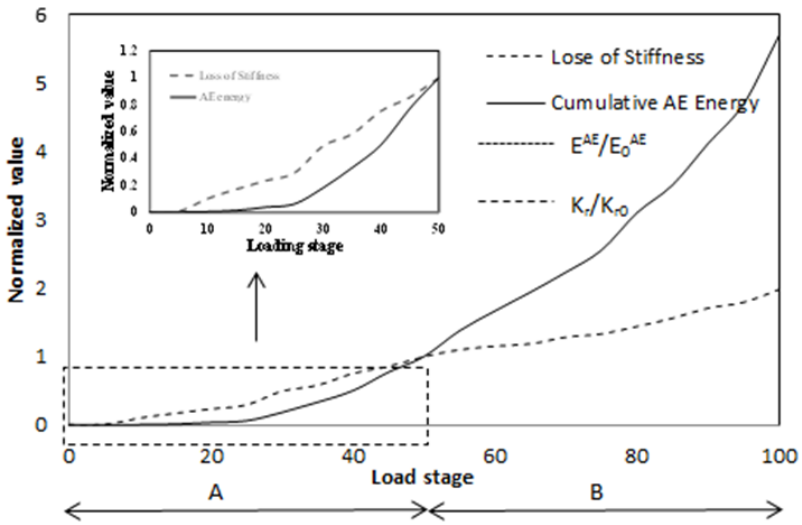

Figure 8. Normalized accumulated AE energy and loss of stiffness at the end of 50% of loading process

a)

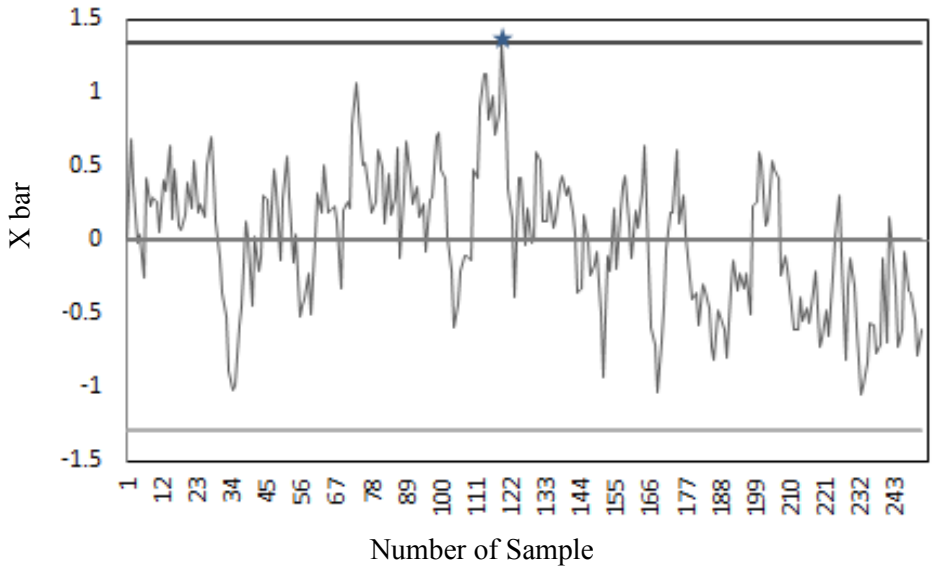
1.5
1
0.5
0
-0.5
-1
-1.5
X bar
1
12
23
34
45
56
67
78
89
100
111
122
133
144
155
166
177
188
199
210
221
232
243
Number of Sample

b)

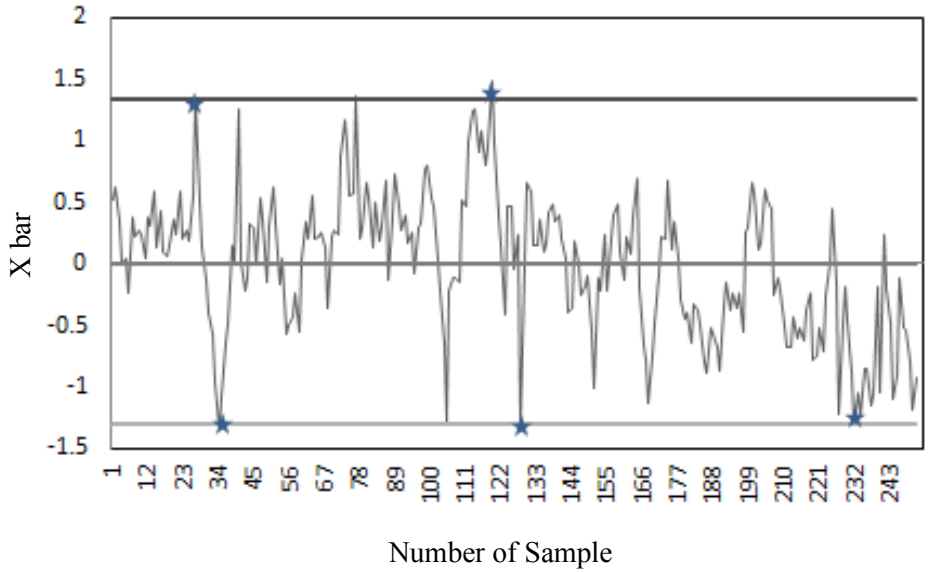
2
1.5
1
0.5
0
-0.5
-1
-1.5
X bar
1
12
23
34
45
56
67
78
89
100
111
122
133
144
155
166
177
188
199
210
221
232
243
Number of Sample

c)

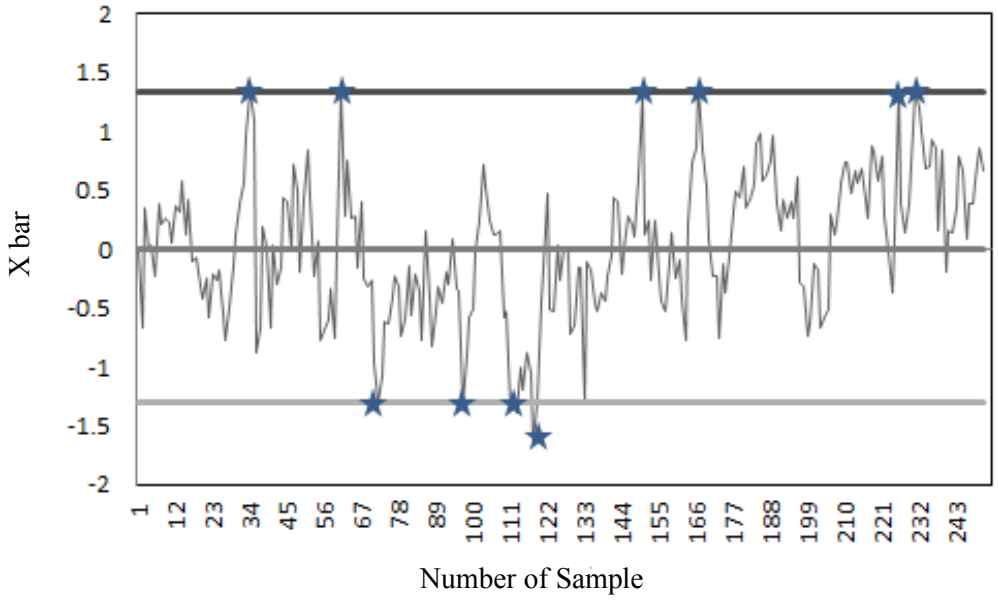

d)

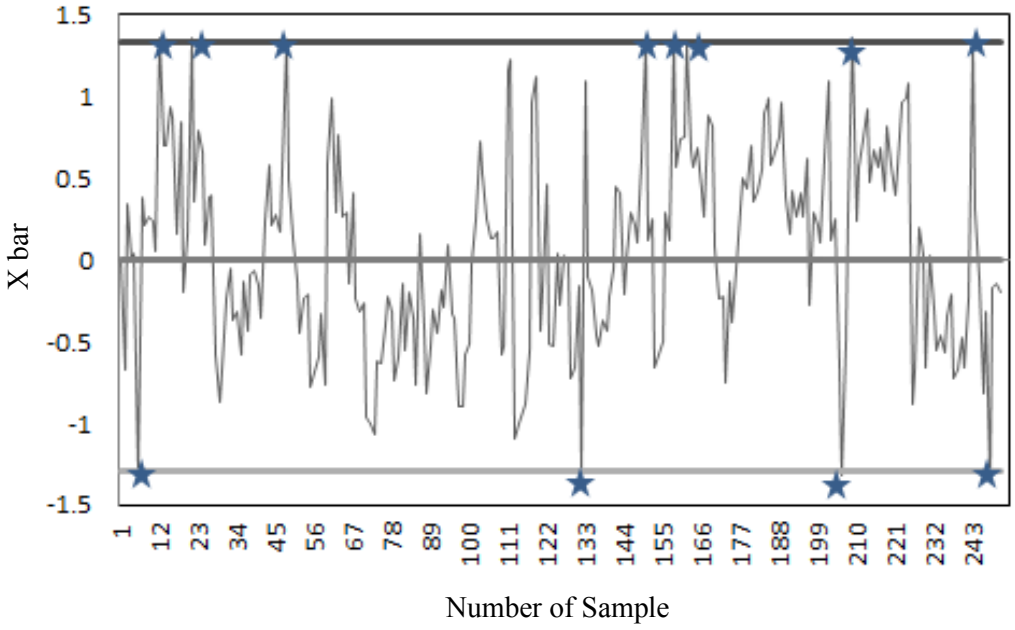

Figure 9: X-bar control chart using first AR coefficient, a) Damage level I (25%), b) Damage level Ⅱ (50%), C) Damage level Ⅲ (75%), d) Damage level Ⅳ (100%)

a)

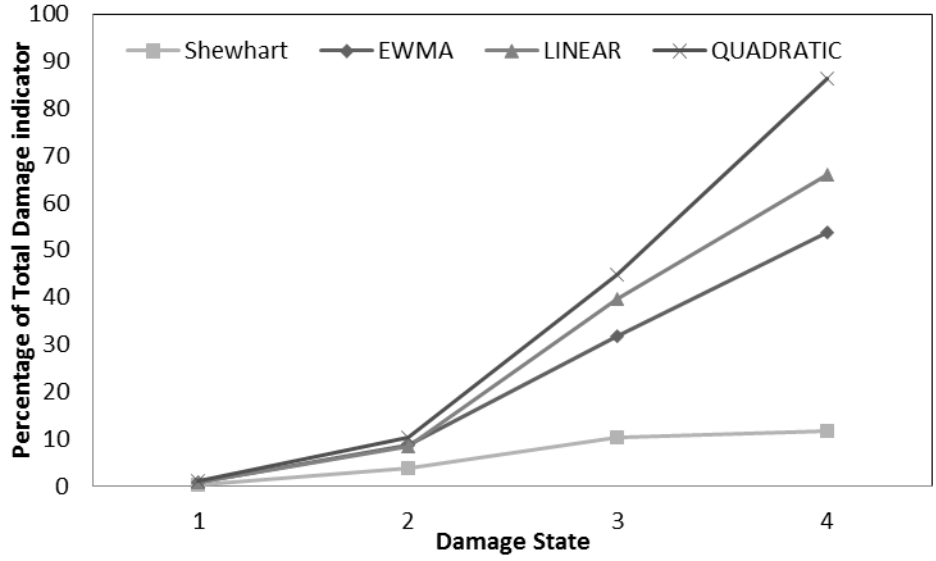

b)

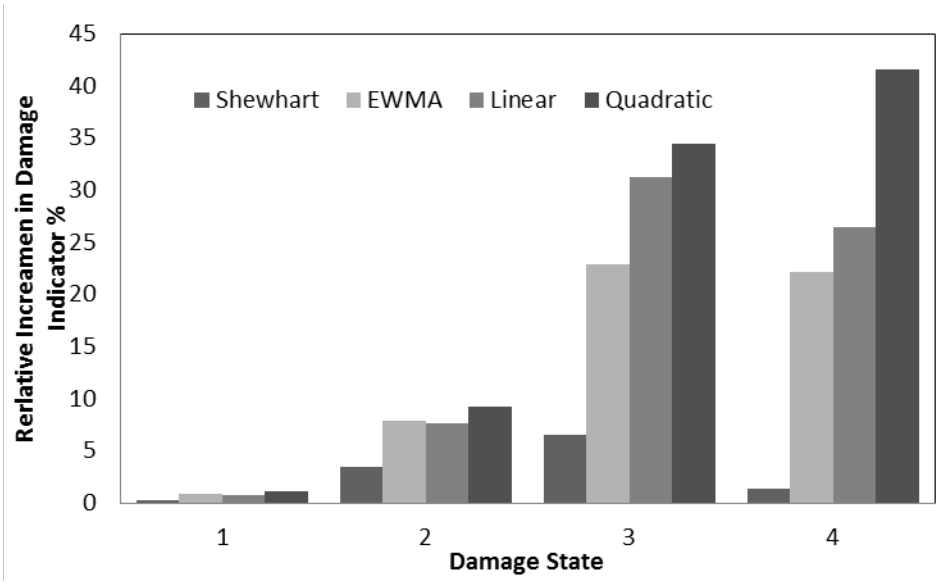

Figure 10: Comparison of structural damage detection schemes: a) Damage sensitivity of different schemes, b) Increment in damage indicator in different schemes

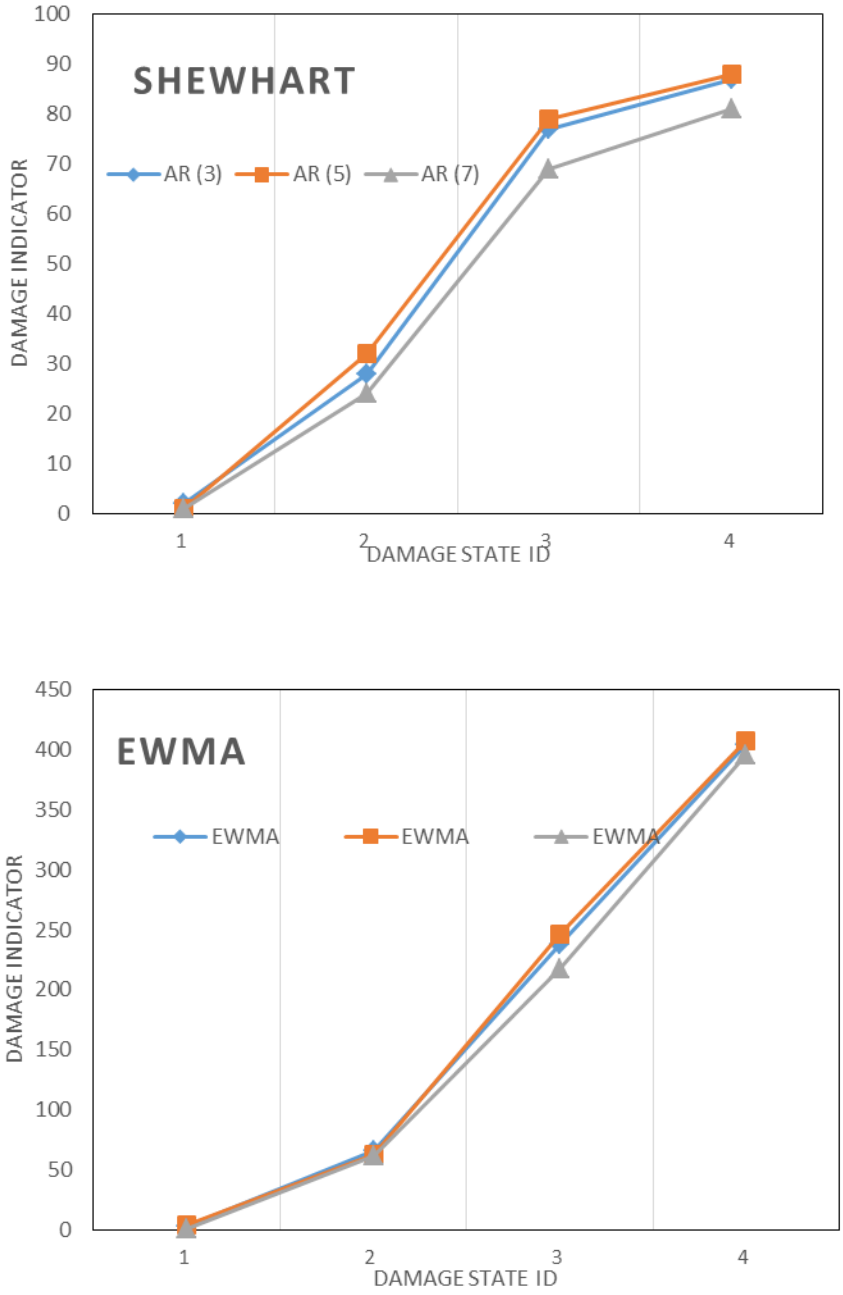

Figure 11: Effect of AR model order on damage indicator sensitivity (order of 3, 5, and7)